Nano Research

Open Access

Research Article

Charge-asymmetry RuCo single atom alloy catalyst for efficient hydrogen evolution reaction

Yi Yao[1], Huilong Geng[2], Wanchun Duan[1], Lili Zhang[3], Faqiang Xu[1] ✉, and Huishan Shang[3] ✉

[1] National Synchrotron Radiation Laboratory (NSRL) University of Science and Technology of China (USTC), Hefei 230029, China
[2] Energy & Catalysis Center, School of Materials Science and Engineering, Beijing Institute of Technology, Beijing 100081, China
[3] School of Chemical Engineering, Zhengzhou University, Zhengzhou 450001, China

Cite this article: *Nano Research*, **2025**, *18*, 94907313. https://doi.org/10.26599/NR.2025.94907313

ABSTRACT: By incorporating a limited number of precious metal atoms into the base metal, the single-atom alloy catalyst not only optimizes the electronic structure and stability of the catalyst but also emerges as an innovative material that enhances the efficiency and selectivity of catalytic reactions. RuCo single-atom alloy electrocatalyst supported on S, N co-doped carbon nanosheets (RuCo SAA/SNC) uniformly distributed on nitrogen, sulfur co-doped carbon nanosheets was prepared by two-step pyrolysis and carbonization. The incorporation of Ru not only optimizes the atomic utilization of Ru but also enhances the charge conduction properties of the surface Co species, thereby increasing the evolution and migration rates of hydrogen ions. In a 0.5 M H_2SO_4 solution, the RuCo SAA/SNC catalyst demonstrates a tafel slope of 27.5 mV·dec^{-1} and an overpotential of merely 43 mV at 10 mA·cm^{-2}. This work achieves enhanced catalytic performance and stability by precisely regulating the atomic-level structure of single-atom alloy catalysts, thereby promoting their widespread application in energy conversion and green chemistry.

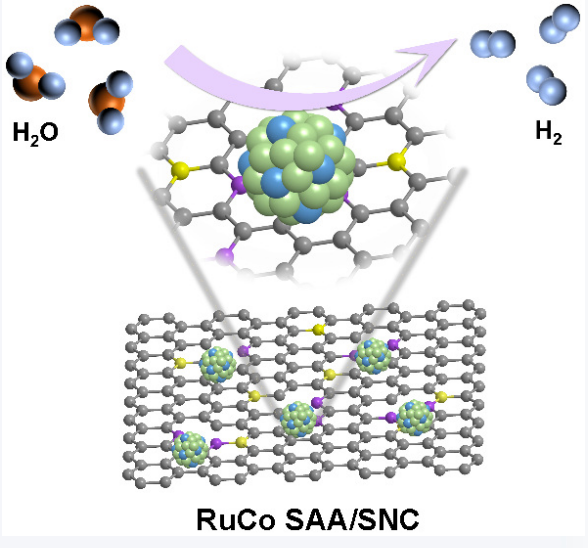

KEYWORDS: single-atom alloy (SAA), atomic regulation, charge asymmetry structure, hydrogen evolution reaction (HER)

1 Introduction

The pursuit of sustainable development in human civilization is driving the shift in the current energy framework. Hydrogen energy is gaining popularity as a sustainable, eco-friendly source due to its wide availability and high calorific value [1–3]. Electrochemical technology provides an efficient method for hydrogen production, offering benefits such as ease of operation, minimal environmental impact, and low energy consumption [4–10]. Currently, the most effective catalysts for the electrochemical hydrogen evolution reaction (HER) continue to be Pt-based precious metal materials. However, their rare availability and high cost of these materials present substantial challenges to the widespread adoption of this technology, hindering the swift progress of the hydrogen economy [11–17]. Thus, minimizing the use of precious metal is a key strategy for developing cost-effective and effective HER catalysts, thereby enhancing the efficiency of water electrolysis for hydrogen production and significantly contributing to the accelerated transformation of the energy system.

Cobalt has emerged as a promising alternative material, demonstrating high activity in the HER process and garnering significant attention [18–22]. Nevertheless, the hydrogen generation efficiency of pure Co species in both acidic and alkaline media requires further enhancement. By alloying and phosphating cobalt's surface to optimize its chemical properties, its hydrogen production efficiency can be significantly improved, while also providing a strong cost advantage in catalysis [23–34]. In the past few years, single-atom catalysts (SACs) have gained significant attention in areas like energy chemistry, biomedical fabrication, and ecological management, owing to their distinctive metal-centered

Received: January 16, 2025; **Revised:** February 13, 2025
Accepted: February 14, 2025

✉Address correspondence to Faqiang Xu, fqxu@ustc.edu.cn; Huishan Shang, shanghs@zzu.edu.cn

coordination structure and optimal atomic utilization [35–43]. However, during the HER, catalyst atoms may migrate or aggregate as a result of excessive reactivity. In contrast, the metal atoms in single-atom alloy (SAA) catalysts offer enhanced stability, reducing the risk of active metal atom loss [44–47]. Single-atom alloy catalysts can effectively regulate the electronic structure of single transition metal atoms by embedding them into the matrix of another metal. Alloyed metal atoms can change the electron density of neighboring atoms through electron effects, so as to optimize the adsorption and dissociation process of hydrogen molecules, and thus improve the activity of HER [48–53]. In addition, compared with the traditional granular catalyst, the single atom alloy catalyst can effectively reduce the presence of non-active regions of the catalyst, thereby improving the catalytic efficiency. Therefore, the design of single atom alloy catalyst to catalyze HER has significant advantages, and is of great significance to promote the development of hydrogen energy economy, which can provide more efficient, stable and economic solutions for energy conversion technology.

In this work, we synthesized the RuCo single-atom alloy catalyst on nitrogen, sulfur co-doped carbon nanosheets (RuCo SAA/SNC) through two-step pyrolysis and carbonization strategy. The results demonstrated that the RuCo SAA/SNC catalysts exhibited remarkable stability and activity for hydrogen evolution during water electrolysis. Especially, the catalytic activity surpasses that of most reported Ru-based HER catalysts. In comparison to pure Co species, the RuCo alloy modified the electronic structure, delivering superior HER performance. Furthermore, the PEM devices was tested in order to promote the real-world application of the RuCo SAA/SNC catalyst. Results indicated that the RuCo SAA/SNC catalyst exhibited superior activity comparable to commercial Pt/C.

2 Experimental

2.1 Synthesis of RuCo SAA/SNC

The SNC nanosheet was first sonicated in 8 mL of ethanol to prepare the RuCo SAA/SNC. Next, to the above suspension, 50 mg of cobaltous nitrate hexahydrate, 10 mg of ruthenium trichloride, 0.15 g of trimesic acid, and 1.2 g of dicyandiamide were introduced and stirred vigorously for 40 min. The solvent was subsequently removed by evaporating the suspension in a rotary evaporator, yielding a grey powder. The powder was then annealed at 900 °C under high-purity nitrogen for 2.5 h with a heating rate of 2 °C·min^{-1}. After natural cooling to room temperature, the black RuCo SAA/SNC was obtained.

2.2 Synthesis of Co NPs SAA/SNC

The NC nanosheet was dispersed in 8 mL of ethanol using ultrasonic treatment. Then, 50 mg of cobalt nitrate hexahydrate, 0.5 mL of thiophene, 0.15 g of caprotriate, and 1.2 g of dicyandiamide were added to the suspension and stirred vigorously for 40 m. The solvent was subsequently evaporated using a rotary evaporator to yield a grey powder. The powder was then heated to 900 °C at a rate of 2 °C·min^{-1} and maintained at this temperature for 2.5 h under a high-purity nitrogen atmosphere. The black Co NPs/SNC was obtained after cooling to room temperature naturally.

2.3 Synthesis of Ru SAC/SNC

RuCo SAA/SNC was prepared by ultrasonically treating SNC nanosheets in 8 mL of ethanol. Subsequently, 10 mg of ruthenium trichloride, 0.15 g of tricaproic acid, and 1.2 g of dicyandiamide were added to the suspension and vigorously stirred for 40 min. The solvent was then removed by evaporating the suspension in a rotary evaporator, yielding a grey powder. The powder was subsequently annealed at 900 °C under high-purity nitrogen for 2.5 h with a heating rate of 2 °C·min^{-1}. After natural cooling to room temperature, black Ru SAC/SNC was obtained.

2.4 Physicochemical characterization.

The crystal phases of each sample were determined through powder X-ray diffraction (XRD), which were recorded using a Bruker D8 Advance diffractometer at a scanning rate of 5 °·min^{-1}. Transmission electron microscopy (TEM) images were captured using a Tecnai G2 F20 S-Twin instrument (FEI Company) operating at an acceleration voltage of 200 kV. For the preparation of the samples, carbon-coated copper grids were immersed in ethanol solutions of the samples and allowed to dry at room temperature before TEM analysis.

2.5 Electrochemical test

Electrochemical measurements were conducted using the CHI 660E three-electrode system. The prepared electrode was tested in a 0.5 M H_2SO_4 aqueous solution, with a platinum sheet as the counter electrode and an Ag/AgCl (saturated KCl) electrode as the reference electrode. A mixture of 5 mg of the sample and 10 μL of 5 wt.% Nafion solution was dispersed in 1 mL of isopropyl alcohol–water (with volume ratio 1:1) solvent by ultrasonic treatment for 20 min to ensure uniform dispersion. Subsequently, 40 μL of the resulting dispersion, containing 10 μg of catalyst, were drop-cast onto a 5 mm diameter glassy carbon electrode, achieving a catalyst loading of 0.204 mg·cm^{-2}. For comparison, a commercial 20 wt.% Pt/C electrode was also prepared. Linear sweep voltammetry (LSV) curves were recorded at a scan rate of 10 mV·s^{-1}, with all potentials referenced to the reversible hydrogen electrode (RHE).

2.6 PEM water electrolyzer test

The catalyst ink was prepared by dispersing the catalyst and 5 wt.% Nafion solution in ethanol, followed by ultrasonication to ensure uniformity. For the catalyst-coated membrane (CCM), the anode catalyst (IrO_2) and cathode catalyst (RuCo SAA/SNC) were individually sprayed onto polytetrafluoroethylene (PTFE) sheets. The PTFE-supported anode and cathode catalysts, along with Nafion 115, were then hot pressed at 120 °C for 5 min under a pressure of 2 T. After the cooling process, the PTFE film on the surface was carefully removed, ensuring that the electrode area of the CCM was 4 cm^2. The catalyst loading was set at 1.0 mg·cm^{-2} for the cathode and 3.0 mg·cm^{-2} for the anode. The prepared CCM was subsequently stored in distilled water for further analysis.

3 Results and discussion

A continuous two-step pyrolysis and carbonization method, illustrated in Fig. 1(a), was demonstrated to effectively introduce a significant number of defects and non-metallic heteroatoms into RuCo SAA/SNC. Exactly, a particular mass ratio of melamine and 2-benzimidazolethiol was initially ground into a uniform mixture, which was then subjected to confined pyrolysis in a flowing inert atmosphere. Due to its high reactivity, the thiol group in 2-benzimidazolethiol was readily extracted by hydrogen to generate

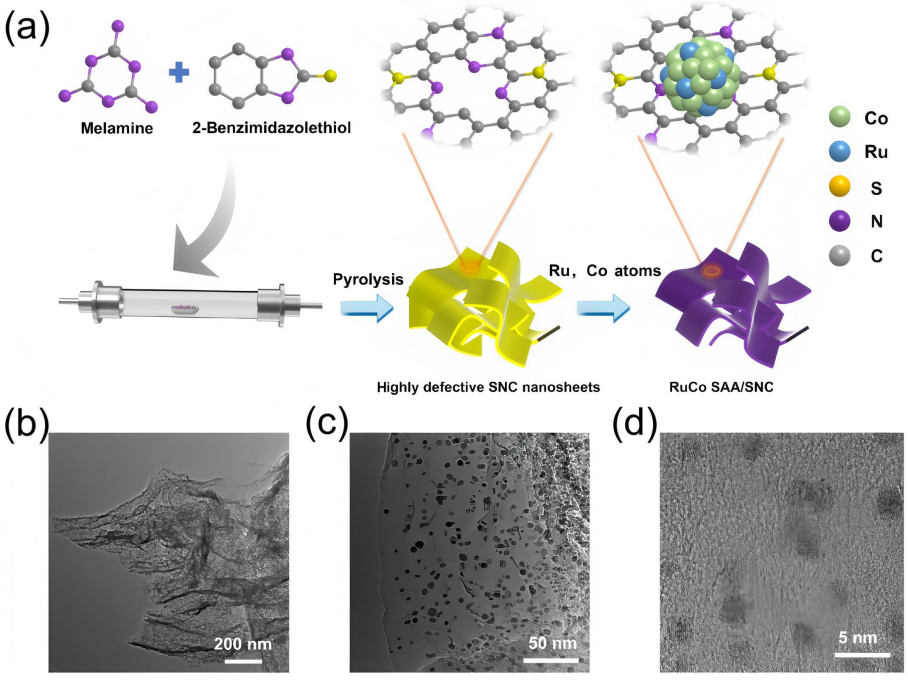

Figure 1 (a) Schematic illustration of synthetic procedure of the RuCo SAA/SNC. TEM images of RuCo SAA/SNC: (b) scale bar: 200 nm and (c) scale bar: 200 nm. (d) High-resolution TEM image of RuCo SAA/SNC.

free radicals. These free radicals facilitated the formation of C–S–C bonds, where the active carbon atom on melamine covalently bonded with the thiol group. At elevated temperatures, melamine converts into a carbon nitride structure (NC), and the polymerization of the NC frameworks leads to the spontaneous formation of numerous defects. During the thermal polymerization of 2-benzimidazolethiol, NC is enclosed through C–S–C bond connections, and the resulting carbon framework undergoes *in situ* restricted pyrolysis, transforming into SNC. In this matrix, sulfur primarily incorporated into the structure as C–S–C bonds. The porous nature of the C-S framework, along with abundance of sulfur-containing sites, promoted the synthesis of catalysts with high loading via defect trapping and sulfur tethering impact. During heating, the edge sulfur sites formed by the cleavage of C–S bonds, along with the nearby nitrogen atoms, effectively anchored individual Ru atoms through sulfur tethering and defect capture. After the initial anchoring, adjacent Ru/Co atoms can shift and engage with each other, leading to the formation of Co–Co/Ru bonds on the graphene substrate surface. Ultimately, RuCo/SNC catalysts were synthesized at specific temperatures through carbonization reduction in an N_2 atmosphere. The mass percentage of Ru and Co in the RuCo SAA/SNC catalyst were determined using inductively coupled plasma-optical emission (ICP-OES), revealing 1.22 wt.% for Ru and 5.07 wt.% for Co (Table S1 in the Electronic Supplementary Material (ESM)).

As illustrated in Fig. S1(a) in the ESM, the morphology of RuCo SAA/SNC was initially examined using scanning electron microscopy (SEM). TEM images revealed that RuCo SAA species are evenly distributed on SNC nanosheets, exhibiting no noticeable aggregation and consistent article size (Fig. 1(b)). TEM image after magnification was shown in Fig. 1(c). The particle size distribution of RuCo SAA is mainly concentrated around 2.7 nm (Fig. S2 in the ESM). It was noted that the inclusion of Ru did not impact the dimension of the Co species, when compared to the TEM image of Co NPs/NC (Fig. S3(a) in the ESM). In addition, we also synthesized Ru SAC/SNC for comparison (Fig. S4 in the ESM). XRD pattern reveals two broad peaks in the 15°–45° range for RuCo SAA/SNC and Co NPs/SNC, corresponding to the (002) and (010) crystal planes of graphitic carbon (Figs. S1(b) and S3(b) in the ESM). XRD findings show that there is no metal peak correlation diffraction, which is speculated to be due to the fact that the insertion of some S atoms reduces the order on the surface of the metal catalyst, making the peak signal not obvious. Soft X-ray absorption near-edge structure (sXAS) spectroscopy was performed to investigate the electronic structure and oxidation states of N and C in the catalysts (Fig. S5 in the ESM). The C K-edge spectrum of RuCo SAA/SNC shows three distinct signals, which are attributed to the π^* (C=C), π^* (C–N/S-Co/Ru), and σ^* (C–C) antibonding orbitals. Besides, three peaks are observed in the N K-edge spectrum of RuCo SAA/SNC, corresponding to pyridine nitrogen, pyrrole nitrogen, and graphite nitrogen. X-ray photoelectron spectroscopy (XPS) was conducted to investigate the chemical composition and electronic structure of RuCo SAA/SNC (Fig. S6 in the ESM). The high-resolution Ru 3p XPS spectrum of RuCo SAA/SNC shows two distinct peaks at 462.1 and 483.9 eV, attributed to metallic Ru^0, while additional peaks at 464.0 and 487.3 eV are assigned to oxidized Ru^{n+} species, further confirming the presence of metallic Ru and individual Ru atoms. Co 2p high-resolution XPS spectra shows a similar pattern.

The atomic-level structure of the prepared RuCo SAA/SNC was further investigate by X-ray absorption spectroscopy (XAS) measurements. Comparison of the XANES spectra of RuCo SAA/SNC with those of Ru foil and RuO_2 reference samples at the Ru K-edge reveals that the absorption edge of RuCo SAA/SNC lies between that of Ru foil and RuO_2, suggesting that the Oxidation state of Ru in RuCo SAA/SNC ranges between 0 and +4 (Fig. 2(a)). Similarly, a comparison of the Co K-edge XANES spectra of RuCo SAA/SNC with those of Co foil and Co_3O_4 reference samples

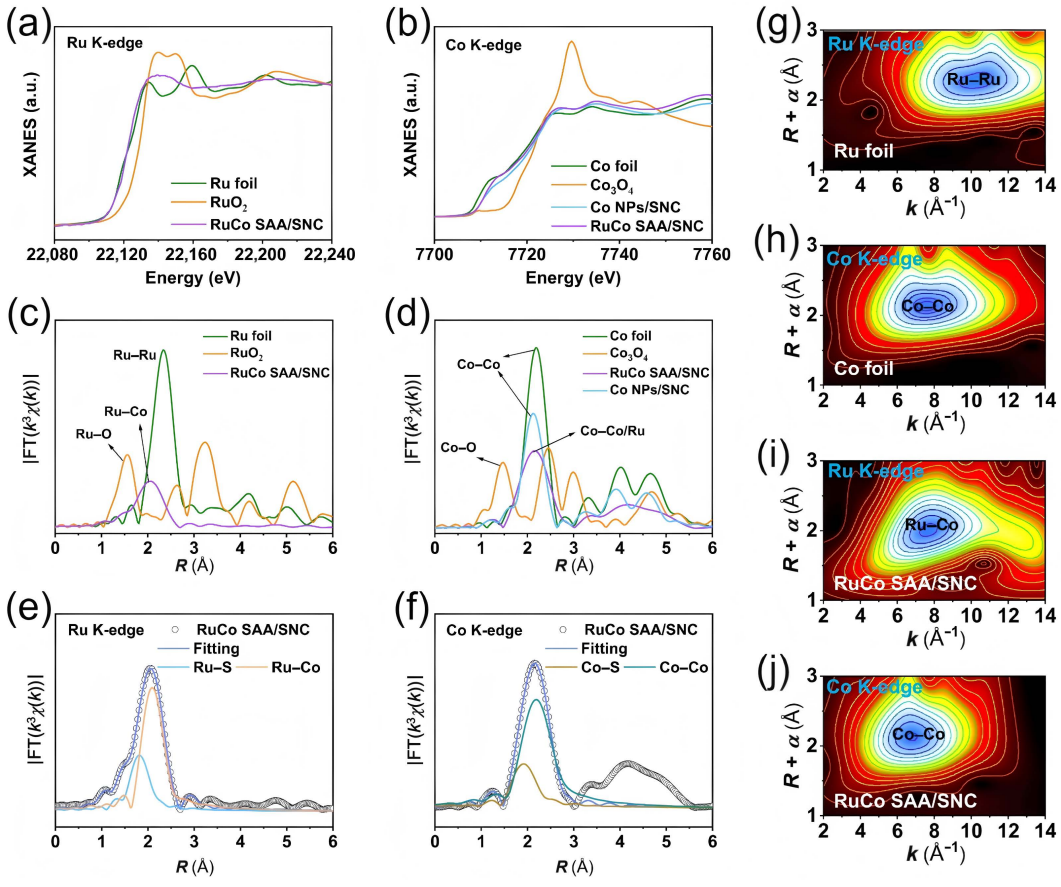

Figure 2 The (a) Ru K-edge and (b) Co K-edge XANES spectra of RuCo SAA/SNC and the references. The FT-EXAFS spectra of RuCo SAA/SNC and the references at (c) Ru K-edge and (d) Co K-edge. The *R* space FT-EXAFS fitting curves of RuCo SAA/SNC at (e) Ru K-edge and (f) Co K-edge. WT-EXAFS plots of (g) Ru foil, (h) Co foil, and RuCo SAA/SNC at (i) Ru K-edge and (j) Co K-edge.

reveals that the oxidation state of Co in the sample is lower than that observed in Co_3O_4 and more closely resembles that of Co foil, suggesting that the oxidation state of Co approaches zero (Fig. 2(b)). According to the first derivative of the absorption edge of RuCo SAA/SNC and references, the valence states of Ru and Co in RuCo SAA/SNC were estimated to be 1.47 and 0.61 (Figs. S7 and S8 in the ESM). The pertinent data from the EXAFS spectrum were extracted and analyzed using Fourier transform (FT). In the Ru K-edge EXAFS spectrum of RuCo SAA/SNC, the absence of a Ru–Ru scattering peak indicates that no agglomerated Ru atoms are present, while Ru–Co signals are observed (Fig. 2(c)). The Co clusters in RuCo SAA/SNC are suggested by the Co–Co signals detected in the EXAFS at the Co K-edge (Fig. 2(d)). Owing to the high resolution in *k* and *R* spaces, the atomically local structure of RuCo SAA/SNC was investigated using wavelet transform (WT)-EXAFS at the Co K-edge and Ru K-edge. The WT images provide additional confirmation of the single Ru atom presence in RuCo SAA/SNC by comparing the strength distribution between metal foil and RuCo SAA/SNC (Figs. 2(g)–2(j), and Figs. S12 and S13 in the ESM).

The best EXAFS fit of RuCo SAA/SNC was obtained by adding Ru/Co–S, Ru–Co, and Co–Co paths (Figs. 2(e) and 2(f), and Fig. S9 in the ESM). The obtained fitting parameters are provided in Tables S2 and S3 in the ESM. Figures S10 and S11 in the ESM display the EXAFS results that best fit for Ru foil and Co foil, demonstrating a good agreement between the fitted curves and experimental spectra. Based on the EXAFS fitting data, the average bond lengths of the first coordination shell for the Ru atom are 0.225 and 0.253 nm, respectively, while the average bond length of the Co–Co bond is 0.256 nm. These findings further suggest that Ru atoms, dispersed at the atomic scale, are randomly arranged across the Co clusters, with some showing partial S-coordination.

The HER catalytic performance of RuCo SAA/SNC and the contrast samples was evaluated in a 0.5 M H_2SO_4 solution, employing a standard three-electrode setup (Fig. S14 in the ESM). Besides, the electrochemical performance of commercial 20% Pt/C catalysts in HER was also evaluated the identical experimental conditions. As illustrated in Fig. 3(a), the RuCo SAA/SNC catalysts exhibit a significantly lower overpotential compared to both Co NPs/NC and Ru SAC/SNC catalysts at the same current density. Specifically, the overpotential of RuCo SAA/SNC can be as low as 43 mV at a current density of 10 mA·cm^{-2}. Moreover, this value is remarkably close to that of commercial Pt/C catalysts. Figure 3(b) shows the Tafel curves of RuCo SAA/SNC, Ru SAC/SNC, Co NPs/SNC, and commercial Pt/C catalysts. It is evident that their tafel slopes are 27.5, 54.2, 84.5, and 37.8 mV·dec^{-1}, respectively. The lower Tafel slope of RuCo SAA/SNC means that the catalyst can more effectively reduce the overpotential of the reaction, thereby increasing its catalytic activity. We supplemented the electrochemical impedance spectroscopy (EIS) test to analyze the charge transfer impedance. The Nyquist diagram indicates that RuCo SAA/SNC exhibits a lower charge transfer resistance

compared to Co NPs/SNC (Fig. S15 in the ESM). To assess the prolonged stability of RuCo SAA/SNC catalysts, its performance was tested through extended cycles. As demonstrated in Fig. S16 in the ESM, there was no significant decline in activity after 5000 cycles. This finding confirms the exceptional durability of RuCo SAA/SNC in enhancing the HER. In acidic solutions, RuCo SAA/SNC demonstrated stable performance in chronopotentiometric tests at a current density of 10 mA·cm^{-2} (Fig. 3(c)). Figure 3(d) and Table S4 in the ESM present a comparison of the HER performance of the RuCo SAA/SNC catalyst with other reported catalysts, highlighting its superior performance. We further tested RuCo SAA's performance in a real PEM electrolyzer. Polarization curves obtained at 60 °C show that RuCo SAA/SNC requires a battery voltage of 1.59 V at 1 A·cm^{-2}, comparable to Pt/C catalysts (Fig. 3(d)). Furthermore, the remarkable stability of the PEM cell underscores the application potential of the RuCo SAA/SNC catalyst. No significant increase in voltage was observed after 30 h of continuous testing at a current density of 1 A·cm^{-2} (Fig. 3(f)). Additional characterizations, including TEM and EXAFS, confirmed that the RuCo SAA/SNC preserved its atomic local structure after the reaction process (Figs. S17 and S18 in the ESM).

To gain a deeper understanding of the structural evolution and mechanism of the catalytic reaction, we employed *in situ* XAS to monitor the catalyst's changes during the catalytic process. The oxidation state of the Ru atom in RuCo SAA/SNC situated between Ru foil and RuO_2, as revealed by the Ru K-edge XANES analysis (Fig. 4(a)). Similarly, the XANES spectrum of the Co K-edge shows similar phenomenon (Fig. 5(a)). Moreover, when the cathode potential is applied, the absorption edge of Ru and Co in RuCo SAA/SNC tends to gradually move towards the lower energy direction, which means that the valence states of Ru and Co decrease with the decrease of the applied potential. In addition, the EXAFS of Ru K-edge and its connectors show that the peak of Ru–Co decreases from 2.09 to 2.07 Å as the reaction progresses, indicating that the Ru–Co bond tends to be compressed (Figs. 4(b)–4(d) and Fig S19 in the ESM). The EXAFS spectra of the Co K-edge show that the Co–Co bond also exhibits a similar phenomenon (Figs. 5(b)–5(d), and Fig. S20 in the ESM). Based on the first derivative analysis of the RuCo SAA/SNC absorption edge (Figs. 5(e) and 5(f)), the characteristic state of Ru decreases from 2.78 to 2.11 as the operating potential is lowered. Likewise, the valence states of Co decreased from 0.53 to 0.40. WT analysis of the EXAFS spectral data confirmed that the overall Ru–Co structure did not change much after exposure to 0.5 M H_2SO_4 electrolyte (Figs. 4(g)–4(i)). The wavelet transform of Co also proves that the structure of Co–Co bond still exists (Figs. 5(g)–5(i)). In summary, the excellent electrocatalytic HER performance of RuCo SAA/SNC results from the combined effect of Co–Co/Ru coordination components. During the HER process, the local coordination environment around the Ru–Co site undergoes slight changes in terms of coordination number and bond length, leading to the formation of a new stable structure. The detection of reaction intermediates at the Ru–Co active site is likely the primary contributing factor.

However, through the parameters obtained by EXAFS fitting (Tables S5 and S6 in the ESM), we found that not only the bond length between atoms changed slightly during HER reaction, but also the coordination number between Ru–Co and Co–Co. As shown in Fig. 6, the coordination number of the catalyst exposed to air is relatively stable before the application of potential. After the application of potential, the local structure of Ru–Co has a subtle change at −0.04 V, and the coordination number becomes smaller to 3.1, and the coordination number continues to decrease when more negative voltage is applied. It is speculated that the change of coordination number is related to the adsorption of active intermediates. The compression of bond length and the change of coordination number can induce the increase of surface partial disorder, thus promoting HER reaction.

4 Conclusions

In this study, a RuCo SAA/SNC catalyst was fabricated through a two-step pyrolysis and carbonization process, showing enhanced HER performance in comparison to the reference samples. The

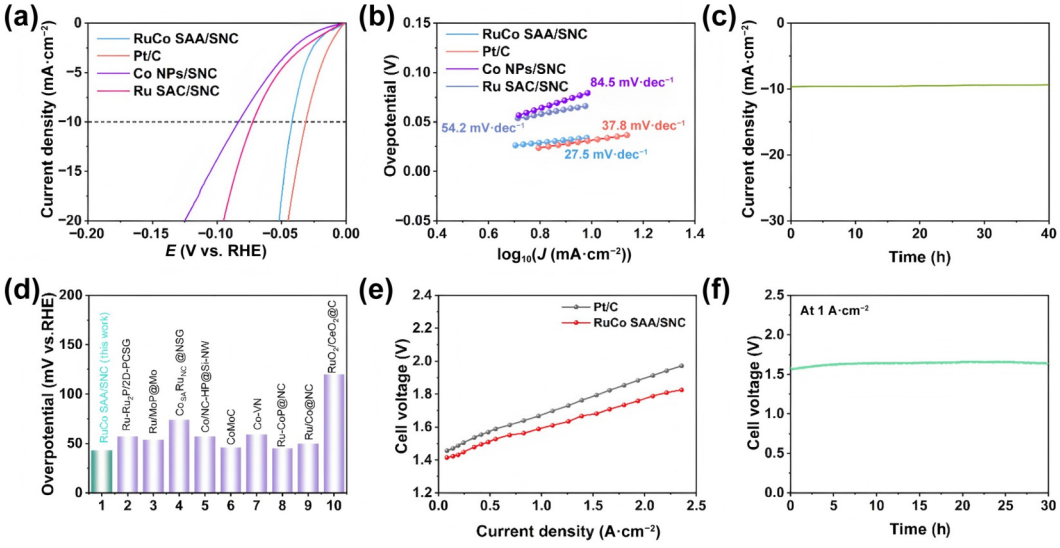

Figure 3 (a) LSV curves of RuCo SAA/SNC, Co NPs/SNC, and commercial Pt/C in 0.5 M H_2SO_4. (b) Tafel plots derived from the polarization curves shown in (a). (c) The chronopotentiometric measurement of RuCo SAA/SNC at the current density of 10 mA·cm^{-2} in acidic media. (d) The overpotential at 10 mA·cm^{-2} for RuCo SAA/SNC compared to other notable catalysts, listed in Table S4 in the ESM. (e) Polarization curves of the PEM electrolysers with RuCo SAA/SNC, and commercial Pt/C as cathode catalysts. (f) Chronopotentiometry curve of the PEM electrolyser with RuCo SAA/SNC as cathode and commercial Pt/C as anode operated at 1 A·cm^{-2}.

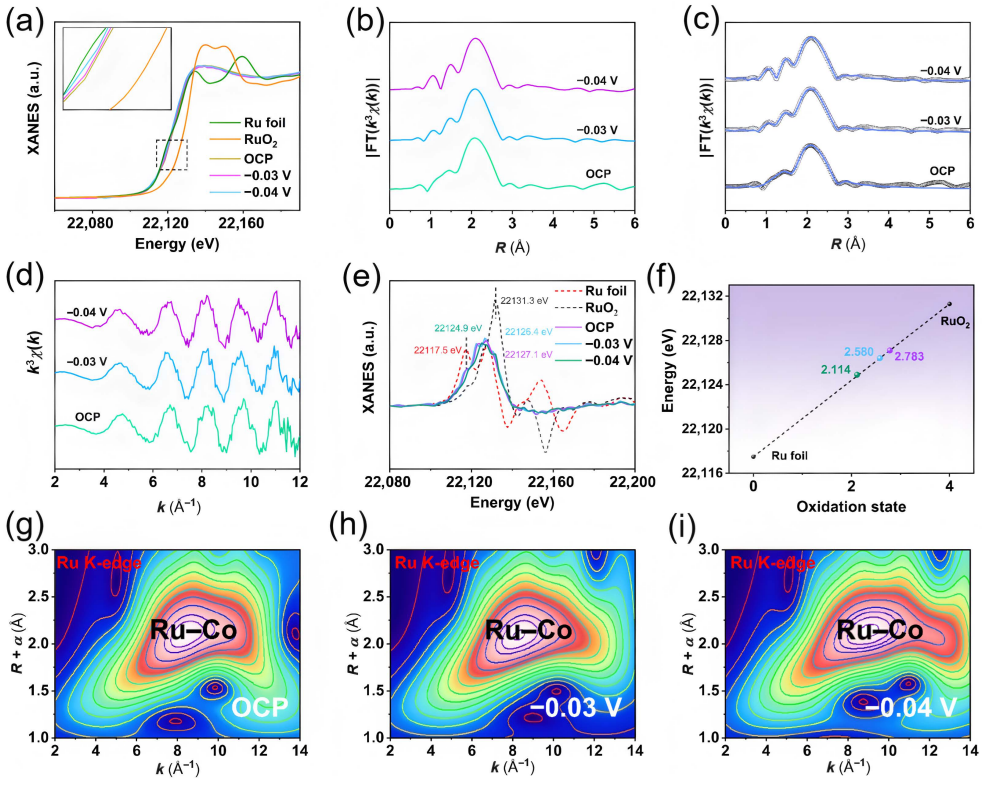

Figure 4 (a) Ru K-edge XANES spectra of RuCo SAA/SNC at various potentials during HER. *In situ* (b) Ru K-edge FT-EXAFS at open circuit, −0.03 V and −0.04 V vs. RHE. (c) EXAFS fitting curves of RuCo SAA/SNC of different potential at Ru K-edge. (d) *In situ* Ru K-edge k^3 FT-EXAFS at open circuit, −0.03 V and −0.04 V vs. RHE. (e) Corresponding first-derivative XANES curves and (f) oxidation state of RuCo SAA/SNC at the Ru K-edge. WT-EXAFS plots of RuCo SAA/SNC at (g) open circuit, (h) −0.03 V, and (i) −0.04 V vs. RHE.

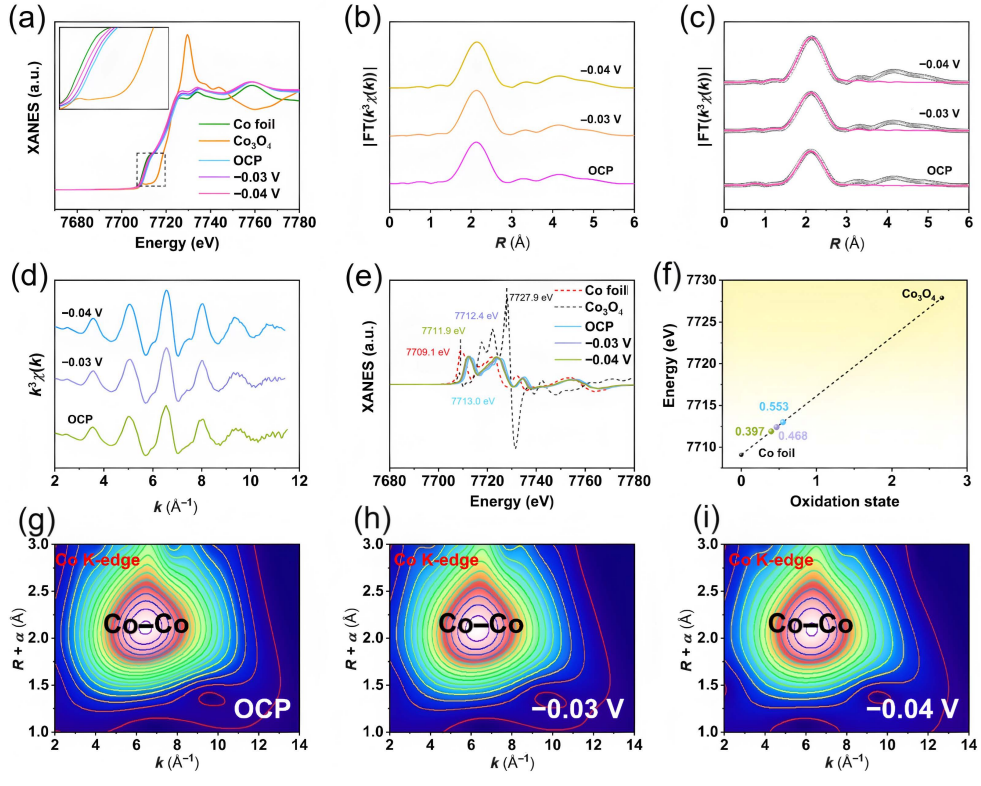

Figure 5 (a) Co K-edge XANES spectra of RuCo SAA/SNC at various potentials during HER. *In situ* (b) Co K-edge FT-EXAFS at open circuit, −0.03 V and −0.04 V vs. RHE. (c) EXAFS fitting curves of RuCo SAA/SNC of different potential at Co K-edge. (d) *In situ* Co K-edge k^3 FT-EXAFS at open circuit, −0.03 V and −0.04 V vs. RHE. (e) Corresponding first-derivative XANES curves and (f) oxidation state of RuCo SAA/SNC at the Co K-edge. WT-EXAFS plots of RuCo SAA/SNC at (g) open circuit, (h) −0.03 V, and (i) −0.04 V vs. RHE.

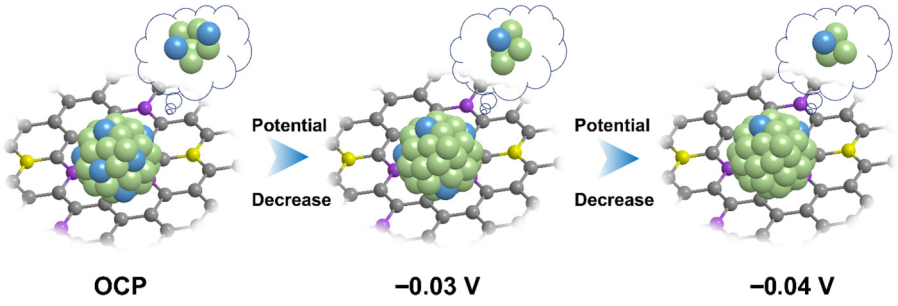

Figure 6 The scheme of catalytically active RuCo SAA is proposed based on operando XAS analysis.

RuCo SAA/SNC catalyst exhibits an overpotential of only 43 mV at a current density of 10 mA·cm^{-2}, with a Tafel slope of 27.5 mV·dec^{-1}, comparable to the commercial 20% Pt/C catalyst. By introducing single Ru atoms, the charge transfer properties of Co species are modified, enhancing hydrogen ion migration rates, while optimizing the utilization of Ru atomic sites. Such a high-efficiency single-atom alloy catalyst design paves the way for new possibilities in clean energy conversion research.

Electronic Supplementary Material: Supplementary material (XAFS measurements, XAFS data processing, TEM, and XRD) is available in the online version of this article at https://doi.org/10.26599/NR.2025.94907313.

Data availability

All data needed to support the conclusions in the paper are presented in the manuscript and the ESM. Additional data related to this paper may be requested from the corresponding author upon request.

Acknowledgements

This work was supported by the National Natural Science Foundation of China (No. 22201262). The authors thank the BL14W1 in the Shanghai Synchrotron Radiation Facility (SSRF) and BL10B and BL12B in the National Synchrotron Radiation Laboratory (NSRL) for help with characterization.

Declaration of competing interest

All the contributing authors report no conflict of interests in this work.

Author contribution statement

Y. Y.: Data curation, writing manuscript. H. L. G.: Data curation, experimental design. W. C. D.: Project administration. L. L. Z.: Project administration, writing manuscript. F. Q. X. and H. S. S.: Project administration, funding acquisition. All the authors have approved the final manuscript.

Use of AI statement

None.

References

[1] Karim, W.; Spreafico, C.; Kleibert, A.; Gobrecht, J.; VandeVondele, J.; Ekinci, Y.; van Bokhoven, J. A. Catalyst support effects on hydrogen spillover. *Nature* **2017**, *541*, 68–71.

[2] Zhou, P.; Navid, I. A.; Ma, Y. J.; Xiao, Y. X.; Wang, P.; Ye, Z. W.; Zhou, B. W.; Sun, K.; Mi, Z. T. Solar-to-hydrogen efficiency of more than 9% in photocatalytic water splitting. *Nature* **2023**, *613*, 66–70.

[3] Boettcher, S. W. Introduction to green hydrogen. *Chem. Rev.* **2024**, *124*, 13095–13098.

[4] Zheng, Y.; Jiao, Y.; Zhu, Y. H.; Li, L. H.; Han, Y.; Chen, Y.; Jaroniec, M.; Qiao, S. Z. High electrocatalytic hydrogen evolution activity of an anomalous ruthenium catalyst. *J. Am. Chem. Soc.* **2016**, *138*, 16174–16181.

[5] Li, J. Y.; Hu, J.; Zhang, M. K.; Gou, W. Y.; Zhang, S.; Chen, Z.; Qu, Y. Q.; Ma, Y. Y. A fundamental viewpoint on the hydrogen spillover phenomenon of electrocatalytic hydrogen evolution. *Nat. Commun.* **2021**, *12*, 3502.

[6] Wang, Y. B.; Lu, Q.; Li, F.; Guan, D. Q.; Bu, Y. F. Atomic-scale configuration enables fast hydrogen migration for electrocatalysis of acidic hydrogen evolution. *Adv. Funct. Mater.* **2023**, *33*, 2213523.

[7] Liao, Y. T.; Zhu, R. T.; Zhang, W. J.; Zhu, H. Y.; Sun, Y.; Chen, J. L.; Dong, Z. H.; Lv, R. H. Transient synthesis of carbon-supported high-entropy alloy sulfide nanoparticles via flash Joule heating for efficient electrocatalytic hydrogen evolution. *Nano Res.* **2024**, *17*, 3379–3389.

[8] Yang, M. Y.; Yuan, J.; Fu, X. L.; Chen, J. J.; Hu, J.; Lu, Z. G.; Liu, C. Surface reconstruction of heterostructures in alkaline medium towards enhanced electrocatalytic hydrogen evolution. *Rare Met.* **2024**, *43*, 2636–2647.

[9] Wang, D. G.; Wu, J. X.; Jiao, L. Y.; Xie, L. M. *In situ* identification of active sites during electrocatalytic hydrogen evolution. *Nano Res.* **2023**, *16*, 12910–12918.

[10] Niu, X. D.; Geng, H. L.; Lv, Z. Y.; Wei, J.; Xu, D. Y.; Chen, W. X. A nitrogen-doped carbon nanosheet composited platinum-cobalt single atom alloy catalyst for effective hydrogen evolution reaction. *Chem. Commun.* **2024**, *60*, 5189–5192.

[11] Wang, C. X.; Guo, W. X.; Chen, T. L.; Lu, W. Y.; Song, Z. Y.; Yan, C. C.; Feng, Y.; Gao, F. M.; Zhang, X. N.; Rao, Y. P. et al. Advanced noble-metal/transition-metal/metal-free electrocatalysts for hydrogen evolution reaction in water-electrolysis for hydrogen production. *Coord. Chem. Rev.* **2024**, *514*, 215899.

[12] Cui, Z. B.; Jiao, W. S.; Huang, Z. Y.; Chen, G. Z.; Zhang, B.; Han, Y. H.; Huang, W. Design and synthesis of noble metal-based alloy electrocatalysts and their application in hydrogen evolution reaction. *Small* **2023**, *19*, 2301465.

[13] Ma, F. Y.; Zhang, P. F.; Zheng, X. B.; Chen, L.; Li, Y. R.; Zhuang, Z. C.; Fan, Y. M.; Jiang, P.; Zhao, H.; Zhang, J. W. et al. Steering the site distance of atomic Cu–Cu pairs by first-shell halogen coordination boosts CO_2-to-C_2 selectivity. *Angew. Chem., Int. Ed.* **2024**, *63*, e202412785.

[14] Li, Q. Q.; Zhang, Q.; Xu, W. L.; Zhao, R.; Jiang, M.; Gao, Y. H.; Zhong, W. D.; Chen, K.; Chen, Y. T.; Li, X. K. et al. Sowing single atom seeds: A versatile strategy for hyper-low noble metal loading to boost hydrogen evolution reaction. *Adv. Energy Mater.* **2023**, *13*, 2203955.

[15] Chen, S. H.; Zheng, X. B.; Zhu, P.; Li, Y. P.; Zhuang, Z. C.; Wu, H. J.; Zhu, J. X.; Xiao, C. H.; Chen, M. Z.; Wang, P. S. et al. Copper

atom pairs stabilize *OCCO dipole toward highly selective CO_2 electroreduction to C_2H_4. *Angew. Chem., Int. Ed.* **2024**, *63*, e202411591.

[16] He, H.; Mai, J. H.; Hu, K. S.; Yu, H. Q.; Zhang, Z. G.; Zhan, F.; Liu, X. H. Recent advances in electrocatalysts for efficient hydrogen evolution reaction. *Rare Met.*, in press, DOI: 10.1007/s12598-024-02649-1.

[17] Fan, M. Y.; Wang, J. J.; Zhao, J.; Zhang, H.; Ma, T. Y.; Han, X. P.; Hu, W. B. High-entropy oxide-supported platinum nanoparticles for efficient hydrogen evolution reaction. *Rare Met.* **2024**, *43*, 1537–1546.

[18] Zhang, X. H.; Wu, A. P.; Wang, D. X.; Jiao, Y. Q.; Yan, H. J.; Jin, C. X.; Xie, Y.; Tian, C. G. Fine-tune the electronic structure in Co–Mo based catalysts to give easily coupled HER and OER catalysts for effective water splitting. *Appl. Catal. B: Environ.* **2023**, *328*, 122474.

[19] Li, S. W.; Ren, P. J.; Yang, C.; Liu, X.; Yin, Z.; Li, W. Z.; Yang, H. J.; Li, J.; Wang, X. P.; Wang, Y. et al. Fe_5C_2 nanoparticles as low-cost HER electrocatalyst: The importance of Co substitution. *Sci. Bull.* **2018**, *63*, 1358–1363.

[20] Jin, Q.; Liu, N.; Dai, C. N.; Xu, R. N.; Wu, B.; Yu, G. Q.; Chen, B. H.; Du, Y. Z. H_2-directing strategy on *in situ* synthesis of Co–MoS_2 with highly expanded interlayer for elegant HER activity and its mechanism. *Adv. Energy Mater.* **2020**, *10*, 2000291.

[21] Wang, X. K.; Zhou, X. K.; Li, C.; Yao, H. X.; Zhang, C. H.; Zhou, J.; Xu, R.; Chu, L.; Wang, H. L.; Gu, M. et al. Asymmetric Co–N_3P_1 trifunctional catalyst with tailored electronic structures enabling boosted activities and corrosion resistance in an uninterrupted seawater splitting system. *Adv. Mater.* **2022**, *34*, 2204021.

[22] Liu, X. H.; Zheng, L. R.; Han, C. X.; Zong, H. X.; Yang, G.; Lin, S. R.; Kumar, A.; Jadhav, A. R.; Tran, N. Q.; Hwang, Y. et al. Identifying the activity origin of a cobalt single-atom catalyst for hydrogen evolution using supervised learning. *Adv. Funct. Mater.* **2021**, *31*, 2100547.

[23] Jung, K.; Pratama, D. S. A.; Haryanto, A.; Jang, J. I.; Kim, H. M.; Kim, J. C.; Lee, C. W.; Kim, D. W. Iridium-cluster-implanted ruthenium phosphide electrocatalyst for hydrogen evolution reaction. *Adv. Fiber Mater.* **2024**, *6*, 158–169.

[24] Banerjee, S.; Kakekhani, A.; Wexler, R. B.; Rappe, A. M. Relationship between the surface reconstruction of nickel phosphides and their activity toward the hydrogen evolution reaction. *ACS Catal.* **2023**, *13*, 4611–4621.

[25] Yu, W. L.; Gao, Y. X.; Chen, Z.; Zhao, Y.; Wu, Z. X.; Wang, L. Strategies on improving the electrocatalytic hydrogen evolution performances of metal phosphides. *Chin. J. Catal.* **2021**, *42*, 1876–1902.

[26] Xu, B. B.; Fu, X. B.; You, X. M.; Zhao, E.; Li, F. F.; Chen, Z. P.; Li, Y. X.; Wang, X. L.; Yao, Y. F. Synergistic promotion of single-atom co surrounding a PtCo alloy based on a g–C_3N_4 nanosheet for overall water splitting. *ACS Catal.* **2022**, *12*, 6958–6967.

[27] Huo, L. X.; Jin, C. Q.; Tang, J. L.; Xu, X. H.; Jiang, K.; Shang, L. Y.; Li, Y. W.; Zhang, J. Z.; Zhu, L. Q.; Chu, J. H. et al. Ultrathin NiPt single-atom alloy for synergistically accelerating alkaline hydrogen evolution. *ACS Appl. Energy Mater.* **2022**, *5*, 15136–15145.

[28] Kayode, G. O.; Hill, A. F.; Montemore, M. M. Bayesian optimization of single-atom alloys and other bimetallics: Efficient screening for alkane transformations, CO_2 reduction, and hydrogen evolution. *J. Mater. Chem. A* **2023**, *11*, 19128–19137.

[29] Wan, R. D.; Luo, M.; Wen, J. B.; Liu, S. L.; Kang, X. W.; Tian, Y. Pt–Co single atom alloy catalysts: Accelerated water dissociation and hydrogen evolution by strain regulation. *J. Energy Chem.* **2022**, *69*, 44–53.

[30] Lv, Y. K.; Han, Y.; Wang, K.; Sun, W. Y.; Du, C. X.; Huang, R. W.; Peng, P.; Zang, S. Q. Satellite Pd single-atom embraced AuPd alloy nanoclusters for enhanced hydrogen evolution. *ACS Nano* **2024**, *18*, 32186–32195.

[31] Han, X. X.; Zhang, L. L.; Wang, X.; Song, S. Y.; Zhang, H. J. Recent progress on the synthesis and applications of high-entropy alloy catalysts. *Nano Res. Energy* **2023**, *2*, e9120084.

[32] Liu, D. Y.; Zeng, Q.; Hu, C. Q.; Chen, D.; Liu, H.; Han, Y. S.; Xu, L.; Zhang, Q. B.; Yang, J. Light doping of tungsten into copper-platinum nanoalloys for boosting their electrocatalytic performance in methanol oxidation. *Nano Res. Energy* **2022**, *1*, 9120017.

[33] Liu, J. W.; Lee, C.; Hu, Y.; Liang, Z. S.; Ji, R.; Soo, X. Y. D.; Zhu, Q.; Yan, Q. Y. Recent progress in intermetallic nanocrystals for electrocatalysis: From binary to ternary to high-entropy intermetallics. *SmartMat* **2023**, *4*, e1210.

[34] Li, Y. P.; Niu, S. W.; Liu, P. G.; Pan, R. R.; Zhang, H. K.; Ahmad, N.; Shi, Y.; Liang, X.; Cheng, M. Y.; Chen, S. H. et al. Ruthenium nanoclusters and single atoms on α–MoC/N-doped carbon achieves low-input/input-free hydrogen evolution via decoupled/coupled hydrazine oxidation. *Angew. Chem., Int. Ed.* **2024**, *63*, e202316755.

[35] Zhang, D. P.; Li, Y. X.; Li, Y.; Zhan, S. H. Towards single-atom photocatalysts for future carbon-neutral application. *SmartMat* **2022**, *3*, 417–446.

[36] Da, Y. M.; Jiang, R.; Tian, Z. L.; Han, X. P.; Chen, W.; Hu, W. B. The applications of single-atom alloys in electrocatalysis: Progress and challenges. *SmartMat* **2023**, *4*, e1136.

[37] Cheng, Y. J.; Wang, H.; Song, H. Q.; Zhang, K.; Waterhouse, G. I. N.; Chang, J. W.; Tang, Z. Y.; Lu, S. Y. Design strategies towards transition metal single atom catalysts for the oxygen reduction reaction-a review. *Nano Res. Energy* **2023**, *2*, e9120082.

[38] Liu, Y.; Zhao, H.; Zhao, Y. L. Designing efficient single metal atom biocatalysts at the atomic structure level. *Angew. Chem., Int. Ed.* **2024**, *63*, e202315933.

[39] Yan, L.; Mao, Y.; Li, Y. X.; Sha, Q. H.; Sun, K.; Li, P. P.; Waterhouse, G. I. N.; Wang, Z. Y.; Tian, S. B.; Sun, X. M. Sublimation transformation synthesis of dual-atom Fe catalysts for efficient oxygen reduction reaction. *Angew. Chem., Int. Ed.* **2025**, *64*, e202413179.

[40] Geng, H. L.; Wei, Z. H.; Li, Y. Q.; Deng, Z. W.; Li, L.; Wang, Y.; Zhai, H. Z.; Li, S. H.; Chen, W. X. Controlling the electron spin states of single-atom catalysts for enhanced electrocatalytic performances. *J. Energy Sustain.* **2024**, *1*, 3630.

[41] Yang, J. R.; Zhu, C. X.; Li, W. H.; Zheng, X. S.; Wang, D. S. Organocatalyst supported by a single-atom support accelerates both electrodes used in the chlor-alkali industry via modification of non-covalent interactions. *Angew. Chem., Int. Ed.* **2024**, *63*, e202314382.

[42] Yang, J. R.; Zhu, C. X.; Wang, D. S. A simple organo-electrocatalysis system for the chlor-related industry. *Angew. Chem., Int. Ed.* **2024**, *63*, e202406883.

[43] Guan, S. Y.; Yuan, Z. L.; Zhao, S. Q.; Zhuang, Z. C.; Zhang, H. H.; Shen, R. F.; Fan, Y. P.; Li, B. J.; Wang, D. S.; Liu, B. Z. Efficient hydrogen generation from ammonia borane hydrolysis on a tandem ruthenium-platinum-titanium catalyst. *Angew. Chem., Int. Ed.* **2024**, *63*, e202408193.

[44] Yan, L.; Wang, D. C.; Li, M.; Lu, R. H.; Lu, M. G.; Li, P. P.; Wang, K. Y.; Jin, S.; Wang, Z. Y.; Tian, S. B. Hexa-atom Pt catalyst fabricated by a ligand engineering strategy for efficient hydrogen oxidation reaction. *Angew. Chem.* **2024**, *136*, e202410832.

[45] Yang, X. F.; Wang, A. Q.; Qiao, B. T.; Li, J.; Liu, J. Y.; Zhang, T. Single-atom catalysts: A new frontier in heterogeneous catalysis. *Acc. Chem. Res.* **2013**, *46*, 1740–1748.

[46] Zhuang, J. H.; Wang, D. S. Recent advances of single-atom alloy catalyst: Properties, synthetic methods and electrocatalytic applications. *Mater. Today Catal.* **2023**, *2*, 100009.

[47] Zhang, Y.; Mu, X. Q.; Liu, Z. Y.; Zhao, H. Y.; Zhuang, Z. C.; Zhang, Y. F.; Mu, S. C.; Liu, S. L.; Wang, D. S.; Dai, Z. H. Twin-distortion modulated ultra-low coordination PtRuNi–O_x catalyst for enhanced hydrogen production from chemical wastewater. *Nat. Commun.* **2024**, *15*, 10149.

[48] Zhang, T. J.; Walsh, A. G.; Yu, J. H.; Zhang, P. Single-atom alloy catalysts: Structural analysis, electronic properties and catalytic

activities. *Chem. Soc. Rev.* **2021**, *50*, 569–588.
[49] Pang, Y.; Wan, X.; Li, Y. C.; Song, M. C.; Liu, X. F.; Shang, J. X.; Zheng, L. R.; Shui, J. L. Evolution of nitrogen-coordinated metal single atoms toward single-atom alloys on MgH_2 as efficient and stable hydrogen spillover catalysts. *Adv. Mater.* **2024**, *36*, 2412942.
[50] Shen, T.; Wang, S.; Zhao, T. H.; Hu, Y. Z.; Wang, D. L. Recent advances of single-atom-alloy for energy electrocatalysis. *Adv. Energy Mater.* **2022**, *12*, 2201823.
[51] Mu, X. Q.; Zhang, X. Y.; Chen, Z. Y.; Gao, Y.; Yu, M.; Chen, D.; Pan, H. Z.; Liu, S. L.; Wang, D. S.; Mu, S. C. Constructing symmetry-mismatched $Ru_xFe_{3-x}O_4$ heterointerface-supported Ru clusters for efficient hydrogen evolution and oxidation reactions. *Nano Lett.* **2024**, *24*, 1015–1023.
[52] Mu, X. Q.; Yu, M.; Liu, X. Y.; Liao, Y. R.; Chen, F. J.; Pan, H. Z.; Chen, Z. Y.; Liu, S. L.; Wang, D. S.; Mu, S. C. High-entropy ultrathin amorphous metal-organic framework-stabilized Ru(Mo) dual-atom sites for water oxidation. *ACS Energy Lett.* **2024**, *9*, 5763–5770.
[53] Hu, Y. M.; Chao, T. T.; Li, Y. P.; Liu, P. G.; Zhao, T. H.; Yu, G.; Chen, C.; Liang, X.; Jin, H. L.; Niu, S. W. et al. Cooperative Ni(Co)–Ru–P sites activate dehydrogenation for hydrazine oxidation assisting self-powered H_2 production. *Angew. Chem., Int. Ed.* **2023**, *62*, e20230880.